Enhanced transport in a porous medium due to dissolved salt

G. Licsandru and M. Prat*
Institut de Mécanique des Fluides de Toulouse (IMFT), Université de Toulouse, CNRS, IMFT, 31400 Toulouse, France

(Received 18 February 2022; accepted 24 May 2022; published 9 June 2022)

An experiment is presented showing enhanced water transport across a porous layer compared to pure water vapor diffusion. The enhanced transport is explained by the presence of brine in the layer and the dependence of the equilibrium vapor pressure with the dissolved salt concentration. The impact of the salt presence is further demonstrated by a comparison with the case of pure water. A significantly longer period of sustained evaporation is obtained in the presence of salt. The transport enhancement effect can last over long periods of time when the conditions are such that the porous layer reaches a dynamic equilibrium between condensation and evaporation. Also, the porous layer can adapt to changes in the boundary conditions via changes in the brine saturation and associated modifications in the salt concentration and the equilibrium vapor pressure. The transport enhancement effect is also illustrated in relation with the dynamics of salt crusts.

DOI: 10.1103/PhysRevFluids.7.064304

I. INTRODUCTION

Evaporation of saline aqueous solutions in porous media is a subject of interest in relation with several important applications, such as evaporation from soils [1], soil salinization [2], or degradation of building materials due to salt crystallization in pores [3], to name only a few. Often, in these applications, the salt presence is considered as negative since it can cause damage [4] or makes soils unsuitable for growing crops [5]. In the present article, we report on an effect of the salt presence, which can be considered as positive since it contributes to the evaporation enhancement compared to the same situation with pure water. The enhancement is attributed to a shortcut effect due to a condensation-evaporation process at the boundaries of the brine clusters present in the porous layer. Enhanced vapor diffusion in a drying porous medium is a long-standing issue in the theory of drying [6]. Phillip and de Vries [7] were the first to introduce a vapor diffusion enhancement factor in their drying continuum model when water vapor diffusion occurs in the presence of liquid water. The enhancement effect is attributed to evaporation-condensation effects in the presence of thermal gradients. Later, the possible significance of evaporation-condensation mechanisms in the presence of thermal gradients was clearly evidenced in microfluidic experiments [8]. The thermal gradients induce a spatial variation of the equilibrium vapor pressure at the surface of the menisci and thus vapor partial pressure gradients. The enhancement is due to condensation at the warmer end of the liquid island followed by evaporation at the cooler end. The end result is that the liquid islands provide a path of reduced resistance that short circuits the normal vapor phase diffusive path which must circumvent the liquid islands [9]. This is quite different from the classical models for vapor diffusion where the liquid islands are obstacles to the vapor phase diffusion path and, thus, hamper the vapor transport with increasing saturation. Accordingly, there should be no enhancement when the temperature is spatially uniform, which is the situation considered in the

*mprat@imft.fr

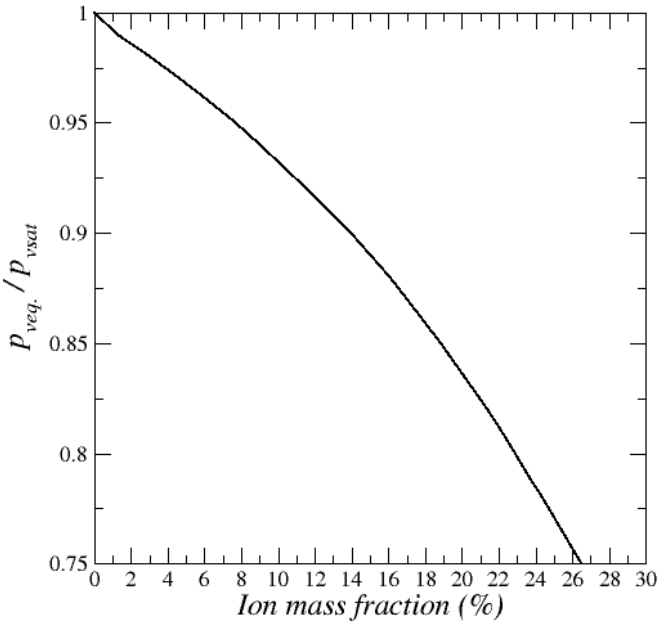

FIG. 1. Variation of water vapor equilibrium pressure as a function of NaCl mass fraction in the NaCl aqueous solution; p_{vsat} is the saturated vapor pressure.

present article. However, the situation is different in the presence of salt and a somewhat similar enhancement effect can be expected in the presence of brine in an isothermal situation since the equilibrium vapor pressure at the interface with an aqueous solution of NaCl depends on the NaCl concentration in the solution (Fig. 1).

As illustrated in Fig. 1, the equilibrium vapor pressure at the surface of a NaCl aqueous solution can vary between the pure water saturated vapor pressure, denoted by p_{vsat}, for a very low salt concentration to 0.75 p_{vsat} for a saturated brine. As a result, condensation-evaporation enhanced transport can be expected when NaCl is present. The objective of the present paper is therefore to present experimental results, analyses, and numerical simulations demonstrating the condensation-evaporation enhanced transport induced by the presence of dissolved NaCl.

The paper is organized as follows. The experiment is presented in Sec. II. Experimental results obtained in the absence of dissolved salt are analyzed in Sec. III. The experimental results with dissolved salt are analyzed in Sec. IV. This is followed by Sec. V in which numerical results are presented considering two main situations: when the liquid phase is percolating and when it is nonpercolating. The impact on the enhanced transport due to the dissolved salt on the dynamics of salt crusts is illustrated in Sec. VI. Section VII consists of the main conclusions of the study.

II. EXPERIMENT

As illustrated in Fig. 2, the experiment is performed in a Hele-Shaw cell connected to a 1 cm diameter cylinder that allows feeding the cell bottom with pure liquid water. The pure liquid water bottom layer is visible in Fig. 2. The Hele-Shaw cell is 60 mm high and 20 mm wide, with an aperture of 2 mm. The cell is rendered hydrophobic by silanization so as to avoid salt creeping on the cell inner walls [10,11], and the development of liquid films along the cell corners; see, e.g., [12]. A suspended porous layer is set in the cell. The procedure for suspending the crust in the cell is delicate and a key aspect of the presented experiment. The method developed to this end is described in Appendix A. The suspended layer is a 3.5 mm thick layer made of glass beads of diameters in the

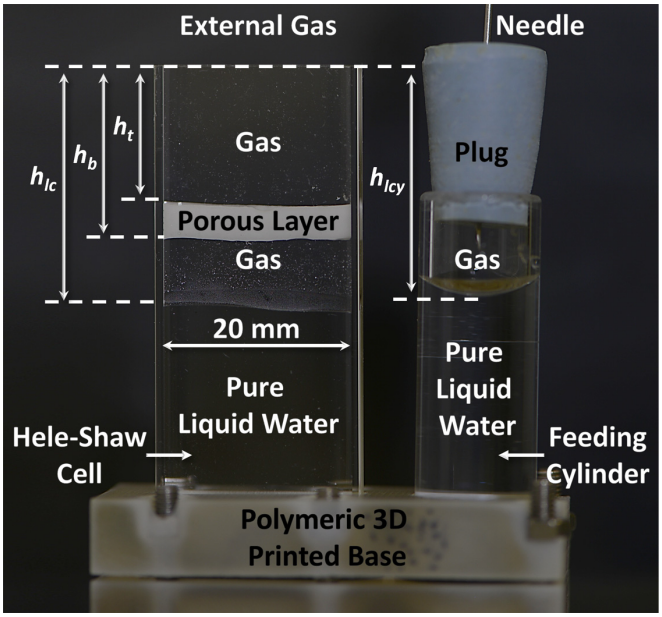

FIG. 2. Experimental setup: Hele-Shaw cell with suspended porous layer. The Hele-Shaw cell is connected to the feeding cylinder on the right via a microchannel in the polymeric base in which the cell and the cylinder are inserted. The Hele-Shaw cell internal width is 20 mm, its aperture is 2 mm, and its height is 60 mm. The feeding cylinder plug is perforated by a needle in order to maintain the gas in the cylinder at the atmospheric pressure.

range 1–50 μm. The Hele-Shaw cell is open at the top. The setup is set in a temperature-controlled enclosure ($\sim$23 °C). Temperature and relative humidity in the enclosure are measured every 1000 s using a Rotronic Hygropalm 2 fitted with a Rotronic Hygroclip SP05 probe. Optical images of the setup are taken every 1000 s with a Nikon D800E camera at a resolution of 7360 × 4912 pixels. From the images, the liquid levels in the cell and the cylinder can be determined every 1000 s as well as the position of the porous layer bottom and top surfaces. The interface positions in the cell considered later in the paper are average positions considering seven vertical lines of pixels evenly distributed over the Hele-Shaw cell width. The mass of the setup is recorded every 100 s with a precision scale (Mettler Toledo AX205 with a readability up to 10^{-5} g). The experiment is performed twice. In the first experiment, referred to as the pure water experiment, the suspended porous layer is saturated with pure liquid water initially. In the second experiment, referred to as the salt experiment, the suspended porous layer is saturated by a NaCl aqueous solution initially. The initial NaCl mass fraction in the solution is 20%, thus relatively close to the solubility (26.4%). In both cases, the relative humidity in the air at the top of the cell is sufficiently low for evaporation to occur. The overall duration of each experiment is 14 days.

TABLE I. Initial positions in the cell for both experiments (see Fig. 2 for definitions).

	Pure water experiment	Salt experiment
Suspended porous layer thickness (mm) ($h_{sl} = h_b – h_t$)	3.4	3.5
$h_t(mm)$	14.7	14.7
$h_b(mm)$	18.2	18.2
$h_{lc}(mm)$	25.4	24.7

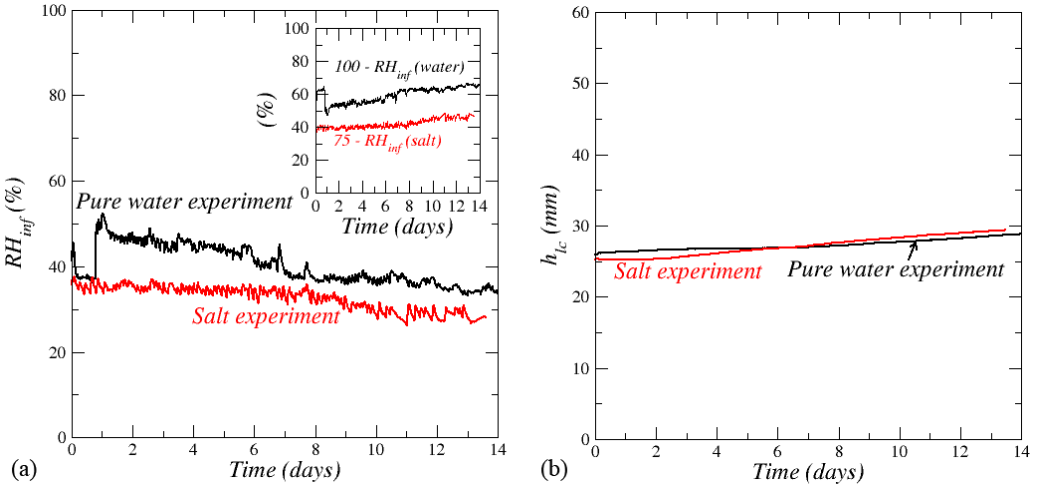

FIG. 3. (a) Relative humidity variations at the cell top in both experiments. The inset shows the relative humidity difference driving the evaporation from a pure water liquid surface and a NaCl saturated solution respectively. (b) Variation of the liquid level in the cell (measured from cell top).

The initial position of the pure water level in the cell and the position of the suspended porous layer are quite close (Table I). As depicted in Fig. 3(a), the relative humidity variation at the top of the cell is slightly different in both experiments. Since the relative humidity at the surface of a salt saturated solution (75%, Fig. 1) is less than for pure water (100%), the relative humidity difference driving the evaporation is also plotted in Fig. 3(a) (inset). As can be seen, the relative humidity difference is higher in the case of the pure water experiment. Figure 3(b) shows that the position of the liquid water level in the cell, which varies due to evaporation, is comparable in both experiments.

A key result is shown in Fig. 4. Figure 4(a) shows the evaporated mass $m(t)$ obtained from the setup weight measurement whereas Fig. 4(b) shows the evaporation rate. The latter is

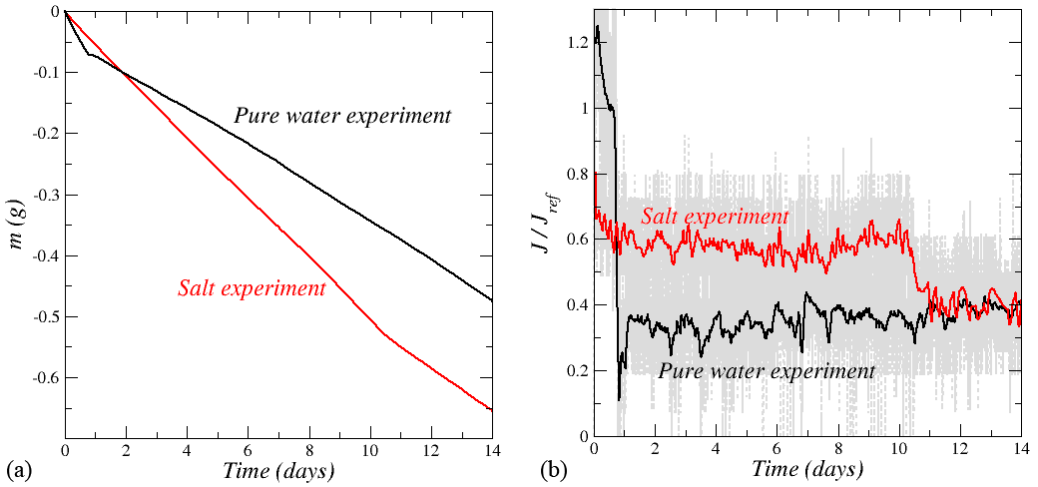

FIG. 4. (a) Evaporated mass as a function of time for both experiments (b) Evaporation rate determined by finite difference from evaporated mass with running average smoothing (see text). J_{ref} is the evaporation rate obtained from Fick's law at the beginning of the pure water experiment.

estimated as follows. The evaporation rate is first estimated from a simple finite difference, $J = -[m(t) - m(t-\Delta t)]/\Delta t$ with $\Delta t = 100$ s. Then the data so obtained are smoothed performing a running average over successive intervals containing 100 values. This leads to the curves in red and black shown in Fig. 4(b). The reference flux in Fig. 4(b) is the flux determined from Fick's law in the case of pure water at the very beginning of the experiment, namely, $J_{\text{ref}} = AD_v \frac{M_v}{RT} p_{\text{vsat}} \frac{(1-\text{RH}_{\text{inf}})}{h_t}$, where D_v is the vapor molecular diffusion coefficient ($D_v \approx 2.7 \times 10^{-5}\,\text{m}^2/\text{s}$), R is the universal gas constant, M_v is the water molecular weight, T is the temperature, A is the cell cross-section surface area, and $p_{\text{vsat}} = 2800$ Pa. As can be seen, except over a short initial period of about 17 h, the evaporation rate is greater by about a factor of 1.6 in the presence of salt over a period of about 9 days leading eventually to an increase of the overall evaporated mass after 10 days of about 50% compared to the pure water case. In spite of the differences in the initial and boundary conditions for both experiments (i.e., mainly the relative humidity at the cell top depicted in Fig. 3), this shows that the salt presence enhances the evaporation and that the effect can be quite significant.

It can also be noticed from Fig. 4(b) that the evaporation rate becomes comparable in both experiments after about day 11. The slight increase over time of the evaporation rate in the pure water experiment is due to the decrease in the external relative humidity shown in Fig. 3(a).

III. PURE WATER EXPERIMENT ANALYSIS

The experiment with pure water can be analyzed as follows by distinguishing two main periods: period 1, corresponding to the short initial period of higher evaporation, and period 2, corresponding to the much longer period of lower evaporation. Initially, the suspended porous layer is saturated with liquid water. Thus, from Fick's law, the evaporation rate can be estimated as

$$J = AD_v \frac{M_v}{RT} p_{\text{vsat}} \frac{(1 - \text{RH}_{\text{inf}})}{h_t}, \tag{1}$$

where RH_{inf} is the relative humidity at the cell top.

From this the evaporated mass variation can be expressed as

$$\frac{dm(t)}{dt} = -AD_v \frac{M_v}{RT} \frac{p_{\text{vsat}}}{h_t} (1 - \text{RH}_{\text{inf}}). \tag{2}$$

The evolution of the evaporated mass is then computed by a simple finite difference approximation as $m(t + \Delta t) = m(t) - AD_v \frac{M_v}{RT} \frac{p_{\text{vsat}}}{h_t} (1 - \text{RH}_{\text{inf}}) \Delta t$.

As can be seen from Fig. 5, the evolution of the evaporated mass so determined, i.e., from Eq. (2), is fully in agreement with the experiment over the first period. Then, the evaporation rate is significantly lower, suggesting that the suspended layer has dried out.

If the suspended layer is assumed to be dry, then the evaporation flux can be estimated from Fick's law as

$$J_{\text{dry}} = A \left(\frac{h_{lc} - h_b}{D_v} + \frac{h_b - h_t}{\varepsilon D_{\text{eff}}} + \frac{h_t}{D_v} \right)^{-1} \frac{M_v}{RT} p_{\text{vsat}} (1 - \text{RH}_{\text{inf}}), \tag{3}$$

where ε is the suspended layer porosity and D_{eff} is the suspended layer effective diffusion coefficient. The latter can be estimated as [13] $D_{\text{eff}} = \tau D_v$ with $\tau \approx \varepsilon^{1/3}$. The evaporated mass m_1 when the curve slope change occurs in Fig. 5(a), i.e., at the end of the first period, is 0.071 g. From this value, one can estimate the suspended porous layer porosity ε from the equation $m_1 = \rho_\ell \varepsilon V$ where ρ_ℓ is the liquid water density and V is the volume of the suspended layer (Table I). This gives $\varepsilon \approx 0.5$. This value seems a bit too high since the layer is formed by a packing of polydisperse beads. For $\varepsilon \approx 0.5$, one obtains $\varepsilon D_{\text{eff}}/D_v \approx 0.4$ using the relationship $\tau \approx \varepsilon^{1/3}$. Then using again the same method as before, i.e., $m(t + \Delta t) = m(t) - J_{\text{dry}} \Delta t$ where J_{dry} is given by Eq. (3), the evaporated mass can be computed. This leads to a somewhat greater evaporated mass compared to the experiment. For this reason, we have proceeded differently and adjusted the coefficient $\varepsilon D_{\text{eff}}/D_v = \varepsilon^{1.33}$. The value $\varepsilon D_{\text{eff}}/D_v = 0.23$ leads to the excellent agreement with the experiment

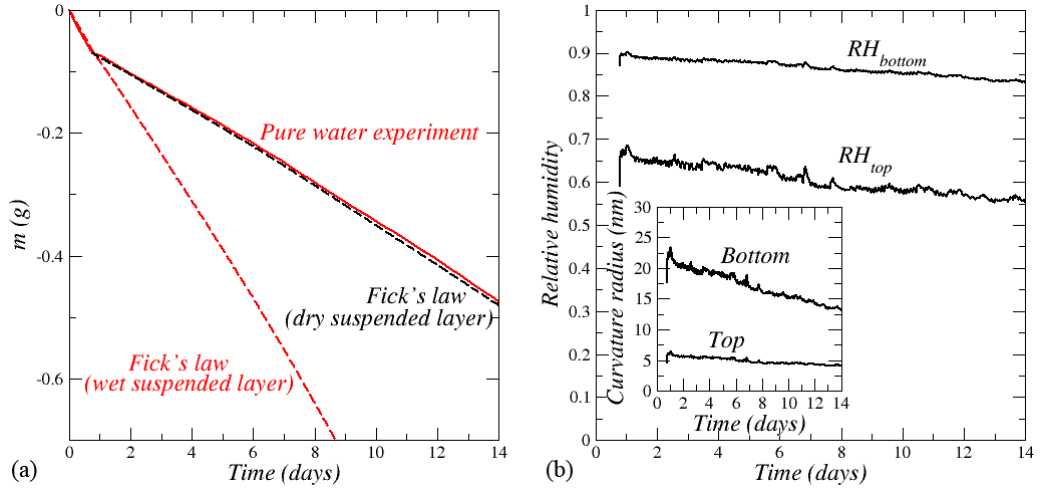

FIG. 5. Pure water experiment: (a) Evaporated mass as a function of time. Comparison with predictions from Fick's law. (b) Computed relative humidity at suspended layer top and bottom surfaces and corresponding meniscus curvature radius according to Kelvin's law (inset).

shown in Fig. 5. This corresponds to an apparent porosity of 0.33 according to the relationship $0.23 = \varepsilon D_{\text{eff}}/D_v = \varepsilon^{1.33}$ [13]. Although a bit high for a polydisperse packing, this value is much more consistent with a random packing of glass beads than the value 0.5 obtained from the evaporated mass in the first period. In fact, we conclude that a film of liquid was present along both sides of the suspended layer at the beginning of the experiment. This explains the too large porosity estimated from the evaporated mass at the end of the first period of greater evaporation. The film thickness e can be estimated from the difference in the evaporated mass at the end of period 1 and the initial mass in the suspended layer assuming the porosity equal to 0.33 and the film present on both sides of the suspended layer, $\rho_\ell 2eA = m_1 - \rho_\ell \varepsilon A h_{sl}$. This gives $e \approx 300\,\mu$m, which is an order of magnitude lower than the suspended layer thickness h_{sl} (Table I). Thus, the presence of liquid film at the beginning of the experiment seems a quite reasonable assumption to reconcile the evaporated mass at the end of period 1 and the porosity estimate.

In any case, the following conclusion is reached: The suspended layer is wet in the first period and evaporation takes place on top of the suspended layer, whereas the suspended layer is dry in the second period and evaporation takes place at the top of the liquid water layer in the cell.

Actually, the suspended crust is not fully dry in the second period. The relative humidities $\text{RH}_{\text{bottom}}$ and RH_{top} at the suspended layer bottom and top surfaces can be computed from Fick's law: $J_{\text{dry}} = AD_v \frac{M_v}{RT} p_{\text{vsat}} \frac{(1-\text{RH}_{\text{bottom}})}{h_{lc}-h_b}$ and $J_{\text{dry}} = AD_v \frac{M_v}{RT} p_{\text{vsat}} \frac{(\text{RH}_{\text{top}}-\text{RH}_{\text{inf}})}{h_t}$ with J_{dry} computed from Eq. (3) with $\varepsilon D_{\text{eff}}/D_v = 0.23$ since this value of $\varepsilon D_{\text{eff}}/D_v$ leads to very good agreement between Eq. (3) and the experimental values. This gives the results shown in Fig. 5(b). Then applying Kelvin's law, $\text{RH} = \exp(-\frac{M_v}{RT}\frac{2\gamma\cos\theta}{\rho_\ell\, r})$, where γ is the surface tension, θ is the contact angle (taken equal to zero), and ρ_ℓ is the liquid water density, allows us to estimate the meniscus curvature radius corresponding to liquid water in equilibrium with the considered relative humidity. As can be seen from Fig. 5, the meniscus radii are in the range 5–20 nm, significantly lower than the smallest beads in the packing ($\sim 1\ \mu$m). Thus, liquid water can be present at the contact points between beads under the form of very small liquid bridges. The corresponding liquid saturation is, however, negligible (even more than considered here since the contact angle is probably greater than zero in our system of hydrophilic but not perfectly wetting glass beads).

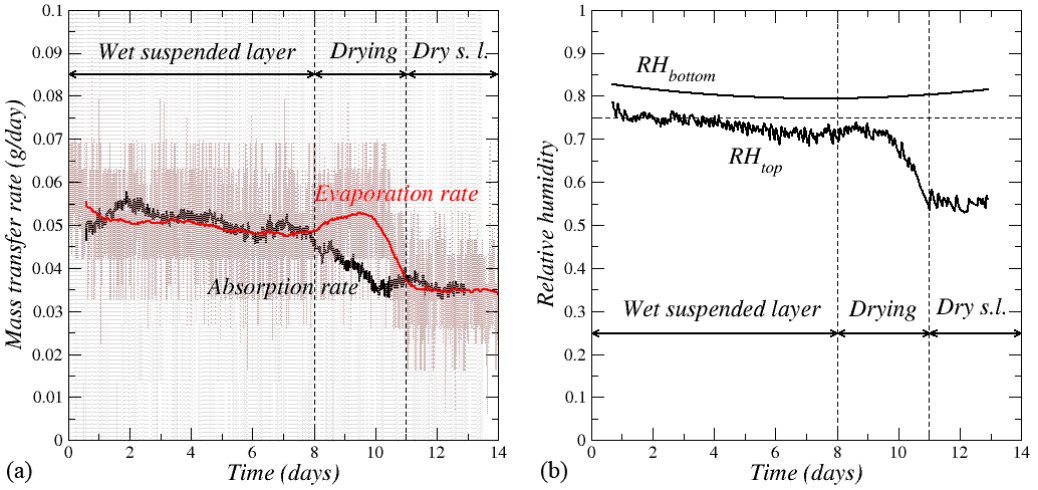

FIG. 6. Salt experiment: (a) Comparison of absorption and evaporation rates; (b) computed evolutions of relative humidity at suspended layer top and bottom surfaces.

IV. SALT EXPERIMENT ANALYSIS

A. Evaporation and absorption rates

Two main periods can be also distinguished in Fig. 4(a) as regards the salt experiment. However, as pointed out in Sec. II, period 1, i.e., the period of greater evaporation, is much longer than with pure water. Since period 1 corresponds to a period in which the suspended layer is wet in the pure water experiment, the suspended layer can also be expected to be wet in period 1 in the salt experiment. Since the suspended layer stays wet over a much longer period, this means that the evaporation rate must be balanced by incoming water. This is possible because the relative humidity in the presence of salt is less than 1 (Fig. 1). This makes possible the mass transfer in the gas phase by vapor diffusion between the pure liquid water layer top at the cell bottom, where the relative humidity is 1, and the suspended layer bottom surface, where $\mathrm{RH}_{\mathrm{bottom}} < 1$ due to the impact of dissolved salt on water activity (Fig. 1). Hence, the variation of the suspended layer saturation, denoted by S, can be expressed as

$$\rho_\ell \mathcal{E} A h_{sl} \frac{dS}{dt} = J_{\mathrm{evap}} - J_{\mathrm{absorp}}, \tag{4}$$

where J_{absorp} is the mass transfer rate between the liquid layer at the bottom and the suspended layer bottom surface. It is referred to as the absorption rate.

This analysis is fully supported by the comparison of the absorption rate and evaporation rate depicted in Fig. 6. The evaporation rate is determined as indicated before by a simple finite difference as $J = -[m(t) - m(t-\Delta t)]/\Delta t$ and the results are then smoothed out by running averages. The difference between Figs. 4(b) and 6 is that the running average was performed over intervals of 100 successive values in Fig. 4 and 1000 values in Fig. 6 for better clarity.

The absorption rate is computed from the variations of the liquid levels in the cell and the adjacent cylinders as

$$J_{\mathrm{absorp}} = -\frac{dm_{\mathrm{level}}}{dt} = -\rho_\ell \left(A \frac{dh_{lc}}{dt} + A_{cyl} \frac{dh_{lcyl.}}{dt} \right), \tag{5}$$

where h_{lcyl} is the liquid level in the feeding cylinder (visible in Fig. 2), A_{cyl} is the cylinder cross-section surface area, and m_{level} is the mass of liquid water at the bottom of the setup (cell and cylinder). The latter is expressed as $A h_{llcell} + A_{cyl} h_{llcyl.}$. The derivatives on the right-hand side of

Eq. (5) are again computed by finite difference as $\frac{dh_{lc}}{dt} = \frac{h_{lc}(t+\Delta t)-h_{lc}\ (t)}{\Delta t}$ (and similar expression for $\frac{dh_{lcyl}}{dt}$). Then the results are smoothed out by running averages using intervals of 100 successive values. This gives the curve in black in Fig. 6(a).

As can be seen, $J_{\text{evap}} \approx J_{\text{absorp}}$ over a long period of 8 days. This indicates that the change in saturation, if any, must be weak over the considered period. The fact that the suspended layer is wet, liquid saturated, or close to liquid saturated, can also be confirmed from the computation of the relative humidity at the suspended layer top and bottom surfaces. From Fick's laws, the evaporation and absorption rates can be expressed as

$$J_{\text{evap}} = AD_v \frac{M_v}{RT} p_{\text{vsat}} \frac{(\text{RH}_{\text{top}} - \text{RH}_{\text{inf}})}{h_t}, \tag{6}$$

$$J_{\text{absorp}} = AD_v \frac{M_v}{RT} p_{\text{vsat}} \frac{(1 - \text{RH}_{\text{bottom}})}{h_{lc} - h_b}. \tag{7}$$

From polynomial fits of the smoothed curves in Fig. 6, applications of Eqs. (6) and (7) lead to the results shown in Fig. 6(b). As can be seen, $\text{RH}_{\text{top}} \approx 0.75$ over the considered period, consistently with a saturated NaCl solution (see Fig. 1). The lower relative humidity at the bottom in this period is compatible with an inhomogeneous distribution of the NaCl mass fraction over the suspended layer thickness as discussed here. Assuming the suspended layer fully saturated, the NaCl mass fraction along the suspended layer thickness is given under steady-state condition by ([14]; see also Appendix B)

$$C(z) = C_{\text{bottom}} \exp\left(\text{Pe}\frac{z}{h_{sl}}\right), \tag{8}$$

where z is a vertical coordinate with $z = 0$ at the suspended layer bottom, h_{sl} is the suspended layer thickness ($h_{sl} = h_b - h_t$), C_{bottom} is the salt mass fraction in the solution at the suspended layer bottom ($z = 0$), and Pe is the Péclet number. The latter is defined as $\text{Pe} = \frac{U_D h_{sl}}{\varepsilon D_s^*}$ where $U_D = \frac{J}{A\rho_\ell}$ is the solution filtration velocity and D_s^* is the ion effective diffusion coefficient ($D_s^* = \tau D_s$ where $D_s = 1.3 \times 10^{-9}\ \text{m}^2/\text{s}$ and $\tau = \varepsilon^{0.33}$ [13]). From the average value of the evaporation rate in Fig. 4(a) (between day 1 and day 8), U_D can be estimated leading to $\text{Pe} = 0.14$. Then assuming that the ion mass fraction corresponds to solubility at the suspended layer top ($C_{\text{top}} \sim 0.264$), one obtains from Eq. (6), $C_{\text{bottom}} \approx 0.23$. As can be seen from Fig. 1, this value corresponds to $\text{RH}_{\text{bottom}} = 0.8$, in good agreement with Fig. 6(b).

The conclusion is therefore that the suspended layer remains saturated with liquid much longer than in the case of pure water thanks to the presence of the salt. The reduced relative humidity in the presence of the salt (roughly 0.75 compared to 1 for pure water) allows us to compensate the water loss by evaporation from the top surface by absorption (condensation) of water on the suspended layer bottom surface. The fact that the suspended layer can be considered as liquid saturated is also consistent with the results presented in Sec. V. Also, considering the steady solution represented by Eq. (8), and not a transient solution, is consistent with the scale characterizing the evolution toward a steady state as presented in Appendix C.

B. Suspended layer is fully dry after day 11

After day 8, the comparison of the evaporation and absorption rates in Fig. 6 indicates that the suspended layer dries in about 3 days between day 8 and day 11 since the evaporation rate is greater than the absorption rate in the corresponding period. Then both rates become similar, which is consistent with a fully dry suspended layer, neglecting the very small amount of solution that can be trapped in the bead contact point regions as discussed in Sec. III for the pure water case. This corresponds to the period after day 11 in Fig. 6. Then the term "absorption" rate used to refer to the mass transfer rate between the liquid surface in the cell and the suspended layer bottom becomes

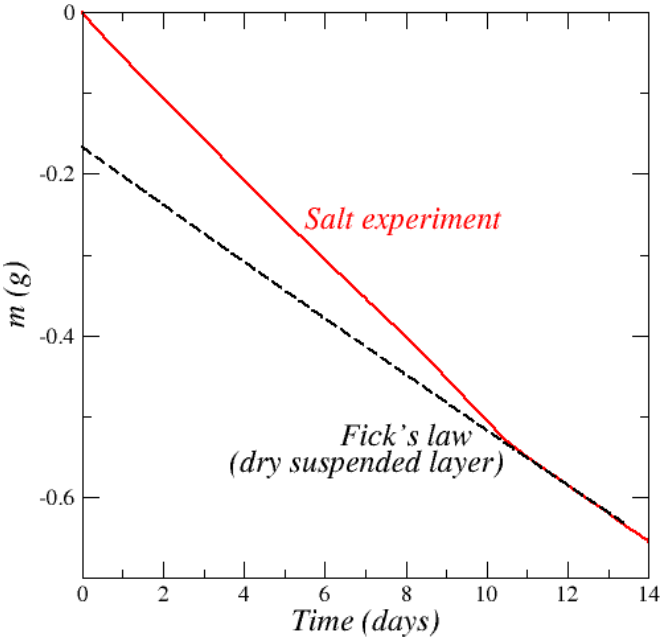

FIG. 7. Evaporated mass as a function of time. Comparison with predictions from Fick's law in the last period.

inadequate in this last period since there is no condensation anymore at the suspended layer bottom. The fact that the suspended layer is fully dry after day 11 can be confirmed by using Eq. (3), Computing the evaporated mass from the equation $m(t + \Delta t) = m(t) - J_{\text{dry}} \Delta t$ where J_{dry} is given by Eq. (3) leads to the result shown in Fig. 7, which is consistent with a fully dry suspended layer after day 11.

As indicated in Fig. 6, the analysis eventually leads to distinguishing three periods rather than two: the long period where the evaporation rate and the absorption rate are comparable and the saturation in the suspended layer is high (wet suspended layer in Fig. 6), the transition period where the evaporation rate is greater than the absorption rate and the suspended layer dries out ("Drying" in Fig. 6), and the last period where the suspended layer is dry ("Dry s.l." in Fig. 6 where "s.l." means suspended layer).

C. Efflorescence formation and disruption of the evaporation-absorption balance

As illustrated in Fig. 8, salt efflorescence forms on top of the glass beads. The efflorescence formation occurs during the drying period between day 8 and day 11. First crystals are detected

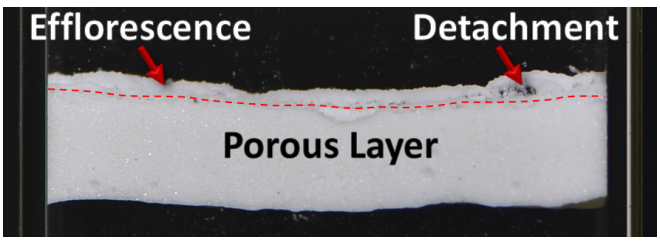

FIG. 8. Salt efflorescence formation over the suspended layer top surface (image at day 11). The red dashed line approximately indicates the suspended glass bead packing (suspended layer) top surface.

at day 8 (when they are at least a few pixels big) and no further efflorescence development occurs after day 11 consistently with a fully dry suspended layer. The average thickness of the efflorescence can be estimated by image processing, leading to $h_{\text{effl}} = 880\,\mu\text{m}$. Assuming the suspended layer fully saturated initially, the mass of salt in the suspended layer is $m_s = \rho_\ell C_0 \varepsilon A h_{sl}$. The corresponding equivalent thickness of crystallized salt when all the salt has precipitated is given by the mass conservation equation $m_s = \rho_\ell C_0 \varepsilon A h_{sl} = \rho_{cr} A h_{effl-eq}$ where ρ_{cr} is the halite density ($\rho_{cr} = 2160\,\text{kg/m}^3$). This gives $h_{effl-eq} = 200\ \mu\text{m}$ for $\varepsilon = 0.5$ (if liquid films are present) and $h_{effl-eq} = 130\ \mu\text{m}$ for $\varepsilon = 0.33$. From these estimates, the porosity of the salt efflorescence can be estimated as $\varepsilon_{\text{effl}} = 1 - \frac{h_{effl-eq}}{h_{\text{effl}}}$. This yields $\varepsilon_{\text{effl}} \approx 0.85$ for $\varepsilon = 0.33$ and $\varepsilon_{\text{effl}} \approx 0.77$ for $\varepsilon = 0.5$. These high values of porosity can be explained as follows.

As can be seen from Fig. 8, the efflorescence tends to detach from the glass bead substrate (this is especially visible on the right of the image). The fact that the efflorescence can detach from the substrate has been reported in [15,16] whereas the upward migration of a precipitated salt layer due to dissolution-precipitation mechanisms has been analyzed in [17,18]. The partial detachment of the efflorescence can thus explain the high apparent efflorescence porosity. Although some precipitation can occur within the top region of the glass bead layer, the conclusion is therefore that the dissolved salt initially in the solution is essentially in the efflorescence which forms during the drying period.

The formation of the efflorescence contributes to further disrupt the balance between evaporation and absorption (condensation) after day 8. The efflorescence is itself a porous material [19,20], with pore sizes expected to be smaller than in the porous substrate (the glass bead packing here) [21,22]. Here, we do not refer to the very big pores or cavities resulting from the efflorescence detachment process (Fig. 8) but to the efflorescence smaller pores. The efflorescence salt crust is therefore wet when it forms. The efflorescence sucks in the solution due to the smaller pores compared to those in the glass bead packing. The solution filling the efflorescence is NaCl saturated. As a result, the evaporation is localized at the top of the efflorescence. The latter being closer to the cell top, the efflorescence formation contributes to enhance the evaporation rate [23] since $J_{\text{evap}} \propto h_t^{-1}$. Note that the efflorescence top surface area remains on the order of the Hele-Shaw cross-section surface area. As a result, the increase in the evaporation rate is essentially controlled by the distance h_t. This is different from situations where the salt structure limiting surface increases significantly as exemplified in [11].

The evaporation rate J_{evap} is also proportional to the relative humidity difference between the efflorescence top surface and the cell top $\text{RH}_{\text{bottom}} - \text{RH}_{\text{inf}}$, where $\text{RH}_{\text{bottom}} \approx 0.75$ (saturated solution in the efflorescence). It can be seen also from Fig. 3 that the difference $0.75 - \text{RH}_{\text{inf}}$ slightly increases between day 8 and day 11. Similarly, according to Fick's law, $J_{\text{absorp}} \propto \frac{(1-\text{RH}_{\text{bottom}})}{(h_{lc}-h_b)}$. The denominator $h_{lc} - h_b$ decreases by a factor of 0.93 between day 8 and day 10 whereas $1 - \text{RH}_{\text{bottom}}$ decreases by a factor 0.86 over the same period due to the slight increase in $\text{RH}_{\text{bottom}}$ [Fig. 6(b)]. This leads to the 20% reduction of the absorption rate in Fig. 6(a) between day 8 and day 10. The slight increase in $\text{RH}_{\text{bottom}}$ can be explained by the migration of the ions toward the efflorescence (as a result, the dissolved salt concentration tends to decrease at the suspended layer bottom) and possibly by the receding of the liquid inside the suspended layer since the solution is sucked in by capillarity into the growing efflorescence.

The conclusion is therefore that the efflorescence formation contributes to further enhance the disruption of the balance between evaporation and absorption, initially induced by the gradual increase in the distance between the liquid level in the cell and the suspended layer bottom surface. This eventually leads to the full drying of the suspended layer and the efflorescence.

Finally, it can be noted that the evaporation rates in both experiments are quite similar in the last period when the suspended layer is dry [after day 11 in Fig. 4(b)] whereas the external relative humidity is lower in the salt experiment [Fig. 3(b)]. This is attributed to the additional resistance to diffusion resulting from the efflorescence formation, see, e.g., [24,25], which here compensates the impact of the lower relative humidity.

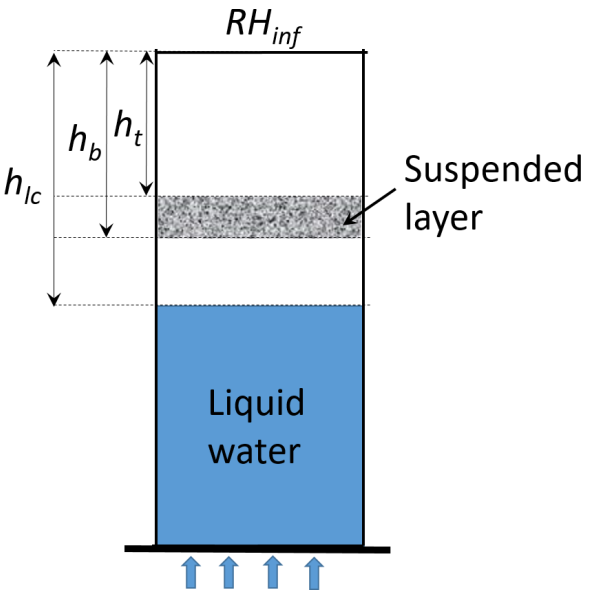

FIG. 9. Evaporation-wicking situation. The cell is continuously fed by water at its bottom.

V. DISCUSSION

In this section, the enhanced transport mechanism is further discussed from simple numerical computations. Also, we discuss whether a similar enhanced transport effect can be expected when the brine is not percolating, a situation also referred to as a pendular state. To this end, the somewhat simpler evaporation-wicking situation depicted in Fig. 10 is considered. This situation is close to the one discussed previously. The difference here is that the liquid water level at some distance below the suspended layer does not recede. It is considered as fixed for simplicity. The lengths in Fig. 9 are similar to the ones in the experiments. For the computations presented below, the following values were considered: $h_t = 17.7$ mm, $h_b = 21.1$ mm, and $h_{lc} = 26.1$. The thickness of the porous layer is $h_{sl} = h_b - h_t = 3.5$ mm.

The objective is to compute the enhancement factor β, characterizing the enhancement of the mass transfer rate compared to the case where the suspended layer is dry. Hence, this factor is defined as

$$\beta = \frac{J}{J_{\text{dry}}}, \tag{9}$$

where J is the mass transfer rate in the considered system whereas J_{dry} [Eq. (3)] is the mass transfer rate assuming that the suspended layer is dry. The layer is supposed fully saturated initially with a NaCl aqueous solution of NaCl mass fraction C_0. Then the saturation is supposed to vary until the equilibrium between the absorption rate [Eq. (7)] and the evaporation rate [Eq. (6)] is reached, i.e., $J = J_{\text{evap}} = J_{\text{absorp}}$. From Eqs. (6) and (7), this condition implies the following relationship between the relative humidities at the bottom and top surfaces of the suspended layer:

$$\text{RH}_{\text{bottom}} = 1 - (\text{RH}_{\text{top}} - \text{RH}_{\text{inf}})\frac{(h_{lc} - h_b)}{h_t}. \tag{10}$$

A. Percolating brine (funicular state)

The steady solution for the situation depicted in Fig. 9 is obtained combining Fick's law, i.e., Eqs. (6) and (7), and the solution to the dissolved salt convection-diffusion equation in the suspended

layer. Regarding the latter, it is first argued that the saturation can be assumed as spatially uniform over the layer because of the expected low value of the capillary number $\mathrm{Ca} = \frac{\mu J \gamma}{A \rho_\ell}$ where γ is the surface tension ($\sim 0.8 \times 10^{-3}$N/m) and μ is the solution dynamic viscosity ($\sim 2 \times 10^{-3}$Pa s). With, for example, $J = J_{\mathrm{evap}} \approx 0.05$ g/day as in the period of higher evaporation rate in the experiment [Fig. 6(a)], this gives $\mathrm{Ca} \sim 10^{-8}$. This very low value indicates that the saturation can be considered as spatially uniform over the layer [26,27]. Under these circumstances, it is shown in Appendix B that the ion mass fractions on the layer top and bottom surfaces are related by

$$C_{\mathrm{top}} = C_{\mathrm{bottom}} \exp(\mathrm{Pe}), \tag{11}$$

where Pe is the Péclet number defined as for Eq. (8) but expressed here as a function of the average interstitial velocity, namely, $\mathrm{Pe} = \frac{U_z h_{sl}}{D_s^*}$ where $U_z = \frac{J}{\rho_\ell \varepsilon S A}$ .C_{top} and C_{bottom} are related to $\mathrm{RH}_{\mathrm{top}}$ and $\mathrm{RH}_{\mathrm{bottom}}$ via the water activity relationship $\varphi(C)$ depicted in Fig. 1, namely, $C_{\mathrm{top}} = \varphi^{-1}(\mathrm{RH}_{\mathrm{top}})$, $C_{\mathrm{bottom}} = \varphi^{-1}(\mathrm{RH}_{\mathrm{bottom}})$.

For a given external relative humidity $\mathrm{RH}_{\mathrm{inf}}$, the solution to the above problem is sought as follows. We search a solution without efflorescence formation. Thus, the relative humidity at the top of the suspended layer cannot be lower than 0.75. Hence, $\mathrm{RH}_{\mathrm{top}}$ must be in the range 0.75–1. The objective is then to determine the saturation S. The algorithm for determining S can be listed as follows:

1) S is varied in the range] S_c, 1]. where S_c is the irreducible saturation. $S_c \approx 0.1$ for a random packing of particles [28].

2) For a given $\mathrm{RH}_{\mathrm{top}}$ the mass transfer rate is computed as $J = J_{\mathrm{evap}} = A D_v \frac{M_v}{RT} p_{\mathrm{vsat}} \frac{(\mathrm{RH}_{\mathrm{top}} - \mathrm{RH}_{\mathrm{inf}})}{h_t}$.

3) $\mathrm{RH}_{\mathrm{bottom}}$ is computed from the condition $J_{\mathrm{absorp}} = J_{\mathrm{bottom}}$, i.e., Eq. (10): $\mathrm{RH}_{\mathrm{bottom}} = 1 - (\mathrm{RH}_{\mathrm{top}} - \mathrm{RH}_{\mathrm{inf}}) \frac{(h_{lc} - h_b)}{h_t}$.

4) The mass transfer rate in vapor phase through the suspended layer is computed as $J_{vap} = A\varepsilon(1-S) D_{\mathrm{eff}} \frac{M_v}{RT} p_{\mathrm{vsat}} \frac{(\mathrm{RH}_{\mathrm{bottom}} - \mathrm{RH}_{\mathrm{top}})}{h_e}$.

5) The mass transfer rate in liquid phase is computed as $J_\ell = J - J_{vap}$.

6) The average interstitial velocity is computed as $U_z = \frac{J_\ell}{A\varepsilon S \rho_\ell}$.

7) C_{top} and C_{bottom} are computed from the activity curve, i.e., $C_{\mathrm{top}} = \varphi^{-1}(\mathrm{RH}_{\mathrm{top}})$, $C_{\mathrm{bottom}} = \varphi^{-1}(\mathrm{RH}_{\mathrm{bottom}})$.

8) The Péclet number is computed from Eq. (11): $C_{\mathrm{top}} = C_{\mathrm{bottom}} \exp(\mathrm{Pe})$, i.e., $\mathrm{Pe} = \log(\frac{C_{\mathrm{top}}}{C_{\mathrm{bottom}}})$.

9) The effective diffusion coefficient D_s^* is determined from $\mathrm{Pe} = \frac{U_z h_{sl}}{D_s^*}$, i.e., $D_s^* = \frac{U_z h_{sl}}{Pe}$.

10) Saturation S_2 corresponding to the computed value of D_s^* is determined from the relationship $D_s^* = (\frac{S_2 - S_c}{1 - S_c}) \tau D_s$ [29], i.e., $S_2 = S_c + (\frac{D_s^*}{\tau D_s})(1 - S_c)$.

11) The difference $\Delta \mathrm{S} = S - S_2$ is computed.

12) The sought solution is the one for which $\Delta \mathrm{S} = 0$.

After convergence, the average ion mass fraction in the layer is computed as $\bar{C} = \frac{1}{h_e} \int_0^{h_e} C dz$, which yields $\bar{C} = \frac{C_{\mathrm{bottom}}}{Pe} [\exp(\mathrm{Pe}) - 1]$ (see Appendix B). Assuming that the layer was initially saturated, the initial ion mass fraction C_0 is determined from the salt mass conservation as $C_0 = \bar{C} S = \frac{S C_{\mathrm{bottom}}}{Pe} [\exp(\mathrm{Pe}) - 1]$.

For simplicity, no supersaturation effect, e.g., [30,31], is considered; i.e., crystallization is expected to occur when $C \approx C_{\mathrm{sat}}$. However, it would be fairly easy to incorporate a supersaturation effect in the algorithm. This will simply modify the lower bounds discussed below. As a result, solutions are sought only for $\mathrm{RH}_{\mathrm{top}} \geqslant 0.75$.

It can be noted that the equation used in step 4 to evaluate J_{vap} is an approximation since the vapor partial pressure does not vary linearly across the layer since C, and thus $\mathrm{RH}_{\mathrm{top}} = \varphi(C)$, does not vary linearly [Eq. (8) and Appendix B]. However, the Péclet number is low in the considered example (Pe $\sim$ 0.1–0.5) and the computations for the considered data show that J_{vap} is negligible compared to J when the saturation is not too low ($S > 0.4$). In other words, the results presented below are only an approximation when the saturation is low. A more refined solution in the range

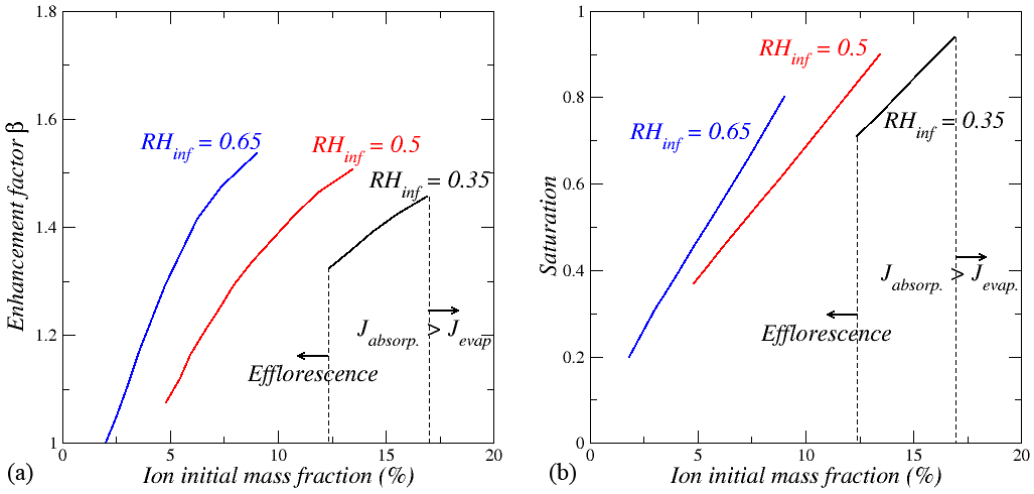

FIG. 10. (a) Variation of the mass transfer rate enhancement factor as a function of the ion initial mass fraction in the layer (supposed fully saturated initially) for three values of the external relative humidity. (b) Variation of the saturation in the suspended layer as a function of the ion initial mass fraction in the layer for three values of the external relative humidity.

of the lower saturations requires a numerical approach to solve the coupled transport equations in the vapor and liquid phases. However, as we shall see, the greater enhancement factors correspond to the greater saturation range, for which J_{vap} is negligible compared to J_ℓ. Although the obtained results are less accurate in the range of the lower saturations, a more refined numerical approach will not change the main trends discussed below.

The above algorithm leads to a solution only for a range of $\mathrm{RH_{top}}$. For instance, solutions are obtained for $\mathrm{RH_{top}}$ in the interval 0.81–0.9 for $\mathrm{RH_{inf}} = 0.65$, 0.75−0.85 for $\mathrm{RH_{inf}} = 0.5$, and 0.75–0.79 for $\mathrm{RH_{inf}} = 0.35$, which correspond to intervals in the initial ion mass fraction C_0. These are indicated in Fig. 10. Let C_{0min} and $C_{0\,\mathrm{max}}$ be the lower and upper bounds of the initial ion mass fraction interval for a given $\mathrm{RH_{inf}}$. As sketched in Fig. 10, crystallization is expected when $C_0 < C_{0\mathrm{min}}$ whereas no solution where $J_{\mathrm{absorp}} = J_{\mathrm{evap}}$ and $S \leqslant 1$ can be found when $C_0 > C_{0\,\mathrm{max}}$. In fact, this means that $J_{\mathrm{absorp}} > J_{\mathrm{evap}}$ when $S = 1$. Thus, a liquid film can form above and below the suspended layer until a steady state is reached (this could be interpreted as a solution for when $S > 1$). For simplicity, this solution has not been explored but the formation of liquid films is *a priori* compatible with a steady-state solution with enhanced mass transfer rate. In other words, considering the liquid film formation should extend the range of solution (on the right side of the curves in Fig. 10). Thus, in what follows, only the situations where $S \leqslant 1$ are considered.

Solutions are illustrated in Fig. 10. As can be seen, the enhancement factor β can be high, up to about 1.5–1.6. From Fig. 4(b), $\beta \approx 1.5$ in the experiment, thus comparable with the highest values computed here. Figure 10 indicates that the higher values of β correspond to the higher values of the initial ion mass fraction, which in turn correspond to high saturations (Fig. 10). In the experiment, this value was 20%. For this value of the initial ion mass fraction, the results shown in Fig. 10 are consistent with a liquid saturated or nearly liquid saturated layer as considered in Sec. IV.

Some overlaps in the initial ion mass fraction intervals can be seen in Fig. 10. This suggests that the system can adapt to changes in the external relative humidity without drying out or salt precipitating if the initial ion mass fraction is adequately specified. This is illustrated in Fig. 11 for $C_0 = 9\%$.

As can be seen, the system adapts to change in $\mathrm{RH_{inf}}$ in the range 0.4–0.7 in this example while maintaining a significant enhancement factor. The adaptation is via change in the saturation and thus in the average ion mass fraction in the layer.

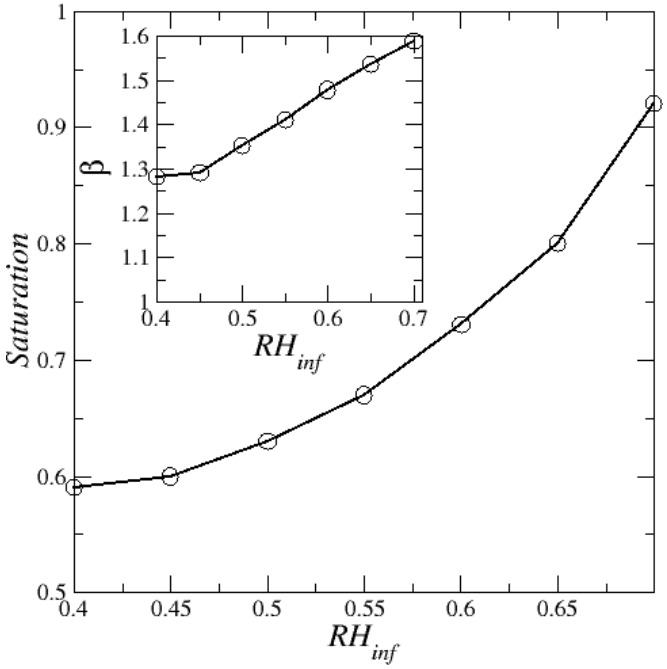

FIG. 11. Variation of saturation and mass transfer rate enhancement factor as a function of external relative humidity for $C_0 = 9\%$.

B. Nonpercolating brine (pendular state)

In this section, it is argued that the liquid phase needs not to be percolating for the enhancement effect to occur over a long period. To this end, the model depicted in Fig. 12, where brine layers alternate with dry layers free of brine, is considered.

Eq. (10) resulting from the condition $J = J_{\text{evap}} = J_{\text{absorp}}$ still holds; namely, $\text{RH}_{\text{bottom}} = 1 - (\text{RH}_{\text{top}} - \text{RH}_{\text{inf}})\frac{(h_{lc}-h_b)}{h_t}$. The ion mass fraction is assumed to be quasiuniform in each wet layer (because of the low Péclet number at the scale of each layer) but varies from one layer to the other. The mass transfer rate can thus also be expressed as

$$J = A\varepsilon D_{\text{eff}} \frac{M_v}{RT} p_{\text{vsat}} \frac{(\text{RH}_k - \text{RH}_{k+1})}{\alpha w}, \tag{12}$$

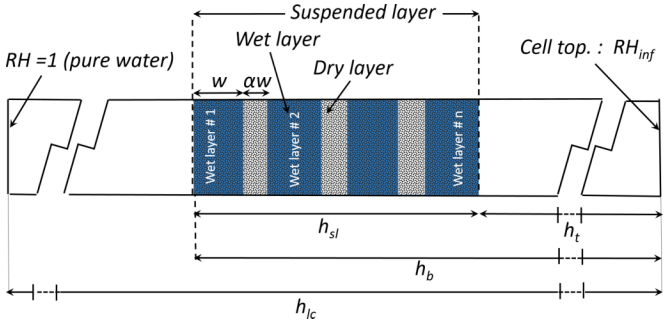

FIG. 12. Simplified brine distribution in the pendular state in the suspended layer. The wet layers are saturated by brine. The salt concentration varies from one wet layer to the other.

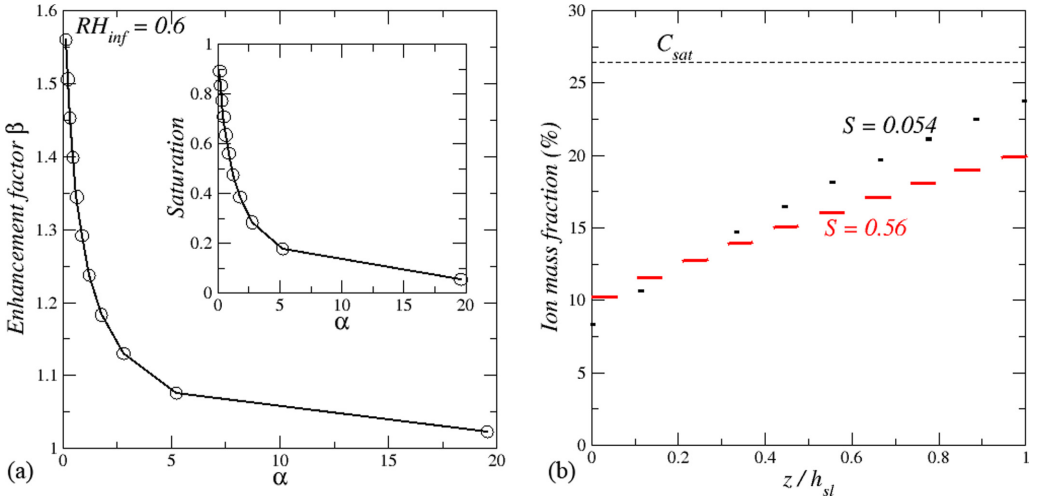

FIG. 13. Nonpercolating liquid phase: (a) Variation of enhancement factor and saturation as a function of α for $\mathrm{RH_{inf}} = 0.6$; (b) ion mass fraction distribution in the wet layer for two saturations and $\mathrm{RH_{inf}} = 0.6$ ($S = 0.054$ and $S = 0.56$ correspond to $\alpha \approx 19$ and $\alpha \approx 0.9$, respectively).

where RH_k is the relative humidity at the boundaries of wet layer number k. The relative humidity differences across the dry layers can thus be expressed from Eq. (12) as

$$\mathrm{RH}_k - \mathrm{RH}_{k+1} = \frac{JRT\alpha\, w}{A\varepsilon D_{\mathrm{eff}} M_v p_{\mathrm{vsat}}}. \tag{13}$$

Summing up Eq. (13) over all the dry layers yields

$$\mathrm{RH}_{\mathrm{bottom}} - \mathrm{RH}_{\mathrm{top}} = \frac{JRT\alpha\, w\,(n-1)}{A\varepsilon D_{\mathrm{eff}} M_v p_{\mathrm{vsat}}}. \tag{14}$$

From the expression of the layer thickness $h_{sl} = nw + (n-1)w$ and Eq. (14), the following relationship is obtained,

$$\alpha = \left(\frac{n}{n-1}\right) \frac{\left(\frac{J_{\mathrm{vap-dry}}}{J}\right)}{1 - \left(\frac{J_{\mathrm{vap-dry}}}{J}\right)}, \tag{15}$$

where $J_{\mathrm{vap-dry}} = \frac{A\varepsilon D_{\mathrm{eff}} M_v p_{\mathrm{vsat}} (\mathrm{RH}_{\mathrm{bottom}} - \mathrm{RH}_{\mathrm{top}})}{RT\ h_e}$ is the mass transfer rate through the layer assumed dry for $\mathrm{RH}_{\mathrm{bottom}}$ and $\mathrm{RH}_{\mathrm{top}}$ imposed at the layer bottom and top boundaries.

The method of solution is as follows. Given values of lengths h_t, h_b, and h_{lc} (the same values as in the percolating case are considered), external relative humidity (i.e., $\mathrm{RH_{inf}}$) and n are specified ($n = 10$ in the results shown below). Then a value for $\mathrm{RH_{top}}$ is selected in the range 0.75–1. J is computed from Eq. (6) and RH_{bottom} from Eq. (10); then α is computed from Eq. (15). The saturation in the layer is computed [$S = \frac{n}{n+(n-1)\alpha}$] as well as the enhancement factor β [Eq. (9)].

Representative results so obtained are shown in Fig. 13. As can be seen, a significant enhancement effect can also be expected in the nonpercolating situation depicted in Fig. 12. However, it can be noticed that the enhancement factor is significant only for relatively high saturations. This suggests that the enhancement effect is small when the pendular state is reached via a classical drying process (for random packing of particles the pendular state is expected for $S < S_c$ with $S_c \approx 0.1$).

Nevertheless, Fig. 13 illustrates a situation where the transfer process is somewhat similar to the one described by Philip and de Vries [7] but due to the ion mass fraction spatial variation

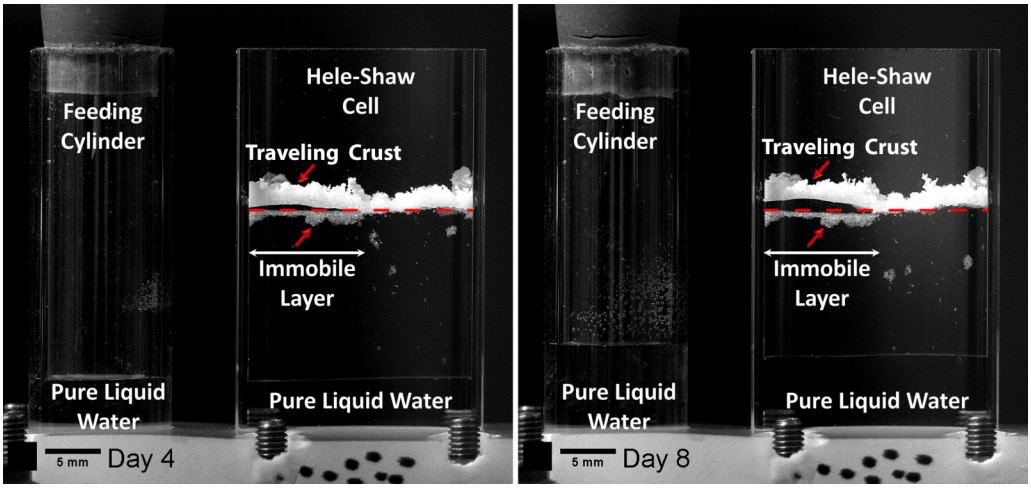

FIG. 14. Experiment with a suspended salt crust in which a layer of glass beads (immobile layer below the red line) is present over only one-half of the cell. The salt crust is above the red line. The elapsed time between the image on the left (day 4) and the image on the right (day 8) is 4 days.

[Fig. 13(b)], and not a thermal gradient. Condensation occurs on the left-hand side of each wet layer in Fig. 12 and evaporation of the right-hand side. The resistance to transport in the layer is only due to the vapor diffusion transport in each dry layer between two wet layers. As a result, the liquid layers act as a shortcut for the water transport.

C. Beyond the Hele-Shaw cell situation

Situations similar to the ones considered in the current study can be expected in the field. For instance, referring to Fig. 9, a possible situation could be the following: the liquid water at the bottom would correspond to the water table (plus the capillary fringe), the suspended layer to a porous layer with brine, and the gas layers above and below the suspended layer to dry porous zones. Also, the enhancement transport effect can contribute to explaining the complex dynamics of salt crusts. As discussed in [15,16], an efflorescence salt crust can detach from the surface of the porous substrate on which it forms initially. When a detached crust is present whereas brine is trapped in the upper region of the porous substrate and is at a lower concentration at some distance below the top region of the porous substrate, the situation is in fact quite close to the one considered in the article. As illustrated in the next section, the enhancement transport effect due to the salt presence can then have an impact on the salt crust dynamics.

VI. ENHANCED TRANSPORT AND SALT CRUST DYNAMICS

As discussed in previous works, e.g., [19,32], the formation of an efflorescence salt crust at the porous medium surface is a major feature of evaporation in the presence of salt. As shown in [15,17], the salt crust is not simply an accumulation of precipitated salt at the porous medium surface. As already mentioned in Sec. IV C, the salt crust can move upward and detach from the porous medium surface. As a result, the understanding of evaporation in the presence of salt crust implies to better understand the salt crust dynamics. The objective in this section is not to address in depth this complex problem, see [17,18], but merely to illustrate the possible impact of the enhanced transport of the salt crust dynamics from a simple experiment.

The experiment is illustrated in Fig. 14. The experimental setup is very similar to the one considered previously in the article (Fig. 2). The main new feature is the presence of a salt crust suspended in the Hele-Shaw cell. One can refer to [17,18] for explanations on how the suspended

crust is obtained. As in the main experiment (Fig. 2), some pure liquid water is injected at the cell bottom, which induces evaporation. As can be seen, a suspended glass bead layer, referred to as the immobile layer in Fig. 14, is present at some distance below the crust. However, it is noteworthy that the immobile layer is present only over the left half of the Hele-Shaw cell whereas the corresponding right half is free of a porous layer, i.e., occupied by the gas phase only. This evaporation situation leads to the upward migration of the salt crust via a combined mechanism of dissolution at the crust bottom and precipitation at the crust top, e.g., [17,18]. As can be seen, the crust upward displacement is significantly greater in the half part of the cell where the immobile layer is present. As discussed in [18], the salt crust displacement speed is proportional to the water absorption rate at the crust bottom surface. Hence, Fig. 14 shows that the absorption rate is greater above the immobile layer than in the region where the immobile layer is not present. If the immobile layer was dry, the opposite would be expected with a greater mass transfer flux and thus a greater crust displacement in the half part where the beads are not present due to the lesser effective diffusion coefficient in the immobile layer compared to free gas. In fact, the immobile layer is partially saturated with brine. As a result of the enhanced transport mechanism analyzed in the article, the crust displacement speed is greater above the immobile layer than in the cell half where the immobile layer is not present.

This simple experiment indicates that the dynamics of salt crust forming at the surface of a porous medium can be significantly affected by the distribution of the brine within the porous medium and illustrates nicely the impact of the enhanced transport mechanism studied in the present article.

To end this section, it can be noted that a reviewer of the present paper original version has suggested that the process of salt crust migration illustrated in Fig. 14 might be related to recent works showing the partial detachments of NaCl crystals from hydrophobic [33] or superhydrophobic surfaces [34]. Nevertheless, our approach of the detachment mechanisms in our experiments, [17,18], is different and does not involve the consideration of interactions between crystals and hydrophobic surfaces. Our motivation is to address situations where detachment occurs in the absence of hydrophobic surfaces as reported, for instance, in [15,16].

VII. CONCLUSION

Water transport mechanisms across a porous layer partially or fully saturated with brine were investigated from a combination of experiments and simple analytical approaches. It was shown that the presence of the brine brings about a short cut effect enhancing the water transport compared to pure water vapor diffusion when the layer is dry. The short cut effect results from condensation-evaporation phenomena at the boundaries of the brine region and the associated flow induced in the brine. The study has demonstrated that a porous layer submitted to vapor gradients at its boundaries can stay wet, i.e., partially brine saturated or nearly saturated, under isothermal conditions over a long period due to the impact of salt on the equilibrium vapor pressure. Such a system can adapt to changes in the boundary conditions by modification of the ion concentration via saturation adaptation so as to reach situations where the condensation rate is balanced by the evaporation rate.

The transport enhancement due to the salt presence was also illustrated through an experiment showing its possible impact on the dynamics of salt crusts.

ACKNOWLEDGMENTS

The financial support from Region Occitanie and Carnot Institut “ISIFOR” is gratefully acknowledged. Authors are grateful to Julien Lefort (IMFT) for his help in the design of the setup and during all the experiments.

APPENDIX A: HOW TO SET A SUSPENDED POROUS LAYER IN A HELE-SHAW CELL

The procedure used to obtain a suspended layer in the Hele-Shaw cell can be outlined as follows. The main steps of the procedure are sketched in Fig. 15.

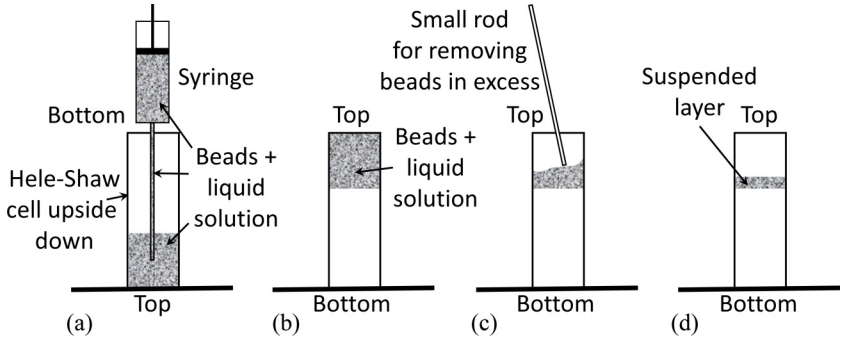

FIG. 15. Schematic of the procedure for suspending the glass bead layer in the Hele-Shaw cell.

As sketched in Fig. 15(a), the Hele-Shaw cell is held upside down in the first step and set on a plate. A mixture of glass beads and solution (at a fixed salt mass fraction) is injected into the cell by means of a syringe up to a level corresponding to the desired suspended layer bottom position while the excess liquid is allowed to leak out of the cell end in contact with the plate. Then, the Hele-Shaw cell is gently set in its normal position. Due to capillary effects and cell hydrophobization, the glass beads stay in the top part of the cell as sketched in Fig. 15(b). The next step [Fig. 15(c)] consists of removing the mixture of glass beads and solution in excess (if needed) so as to obtain the desired porous layer thickness. This is performed gradually by means of a small rod allowing the removal of a small amount of the mixture every time. The final step (not shown) before the experiment is launched consists of perforating the porous layer with a very small needle. Once the needle is in place, liquid water is set in the cell bottom up to a desired level by injecting water in the feeding cylinder (Fig. 2). The role of the needle is to avoid the gas compression underneath the porous layer when the liquid water is injected. Once the liquid water at the cell bottom has reached the desired level, the needle is removed and the porous media gently vibrated so that the hole remains. Then the experiment can start.

APPENDIX B: STEADY-STATE SOLUTION TO THE DISSOLVED SALT TRANSPORT EQUATION

Within the framework of the continuum approach to porous media, the equation governing the ion mass fraction in the layer can be expressed as [35,36]

$$\varepsilon\frac{\partial\rho_\ell SC}{\partial t}+\frac{\partial}{\partial z}(\rho_\ell\varepsilon SU_zC)=\frac{\partial}{\partial z}\left(\rho_\ell\varepsilon SD_s^*\frac{\partial C}{\partial z}\right), \tag{B1}$$

where U_z is the average interstitial velocity of the solution. When the saturation is spatially uniform in the steady-state regime, Eq. (B1) reduces to

$$\rho_\ell\varepsilon SU_z\frac{\partial C}{\partial z}=\rho_\ell\varepsilon SD_s^*\frac{\partial^2 C}{\partial z^2}, \tag{B2}$$

and thus to

$$U_z\frac{\partial C}{\partial z}=D_s^*\frac{\partial^2 C}{\partial z^2}, \tag{B3}$$

which can be solved to obtain

$$C=C_{\text{bottom}}\exp\left(\text{Pe}\frac{z}{h_{sl}}\right), \tag{B4}$$

where $\mathrm{Pe} = \frac{U_z h_{sl}}{D_s^*}$. The corresponding average ion mass fraction in the layer can be determined from Eq. (B4) as

$$\bar{C} = \frac{1}{h_{sl}} \int_0^{h_{sl}} C dz = C_{\text{bottom}} \frac{1}{h_{sl}} \int_0^{h_{sl}} \exp\left(\mathrm{Pe}\frac{z}{h_{sl}}\right) dz = \frac{C_{\text{bottom}}}{Pe} \left[\exp\left(\mathrm{Pe}\frac{z}{h_e}\right)\right]_0^{h_{sl}}, \tag{B5}$$

which gives

$$\bar{C} = \frac{C_{\text{bottom}}}{Pe}[\exp(\mathrm{Pe}) - 1]. \tag{B6}$$

APPENDIX C: TIMESCALE

A characteristic time to reach the steady-state distribution, given by Eq. (B4), starting from a uniform distribution of the initial ion mass fraction, denoted by C_0, can be obtained as follows. While the origin of z ($z = 0$) is at the bottom of the layer with Eq. (B4), the origin is considered in the middle of the layer in what follows. The distribution is considered as antisymmetrical about the plane $z = 0$ (the increase in the salt mass fraction in the region $0 \leqslant z \leqslant h_{sl}/2$ due to the advective transport is balanced by the decrease in the salt mass fraction in the region $\frac{-h_{sl}}{2} \leqslant z \leqslant 0$). Then the solution at intermediate times in the upper half of the layer is expressed as

$$C = C_0 \exp\left(\frac{U_z[z - \delta(t)]}{D_s^*}\right) \delta(t) \leqslant z \leqslant h_{sl}/2, \quad C = C_0 \text{ for } 0 \leqslant z \leqslant \delta(t). \tag{C1}$$

The next step is to express that the growth of the region where the mass fraction is in excess (i.e., above C_0) results from the incoming adjective mass transfer rate, $J_s = \rho_\ell \varepsilon S C_0 U_z A$. Thus,

$$J_s t = \rho_\ell \varepsilon S C_0 U_z A t = \rho_\ell \varepsilon S A \left\{ \int_{\delta(t)}^{h_{sl}/2} C_0 \exp\left(\frac{U_z[z - \delta(t)]}{D_s^*}\right) dz - \left[\frac{h_{sl}}{2} - \delta(t)\right] C_0 \right\}, \tag{C2}$$

which gives

$$\rho_\ell \varepsilon S C_0 U_z A t = \rho_\ell \varepsilon S A C_0 \left(\frac{D_s^*}{U_z} \left\{ \exp\left[\frac{U_z\left(\frac{h_{sl}}{2} - \delta(t)\right)}{D_s^*} \right] - 1 \right\} - \left(\frac{h_{sl}}{2} - \delta(t) \right) \right). \tag{C3}$$

In our study, the Péclet number is small (∼0.1–0.5). Using a second order Taylor expansion of the exponential term in Eq. (C3) gives

$$\rho_\ell \varepsilon S C_0 U_z A t = \rho_\ell \varepsilon S A C_0 \left\{ \frac{D_s^*}{2U_z} \left[\frac{U_z\left(\frac{h_{sl}}{2} - \delta(t)\right)}{D_s^*} \right]^2 \right\}, \tag{C4}$$

$$\rho_\ell \varepsilon S C_0 U_z A t = \rho_\ell \varepsilon S A C_0 \left[\frac{U_z}{2D_s^*} \left(\frac{h_{sl}}{2} - \delta(t) \right)^2 \right], \tag{C5}$$

from which the desired characteristic time can be estimated as [when $\delta(t) = 0$]

$$t_{ch} = \frac{h_{sl}^2}{8D_s^*}, \tag{C6}$$

which finally is nothing else than a classical characteristic diffusion time (low Péclet number limit). For $S = 1$, Eq. (C6) gives $t_{ch} \approx$ 30 min. This time is short compared to the duration of the long period [8 days in Fig. 6(a)] before the first crystals are detected and where $J_{\text{evap}} \approx J_{\text{absorp}}$. Thus considering a steady-state solution in Sec. IV A is quite reasonable.

[1] X. Y. Chen, Evaporation from a salt-encrusted sediment surface: Field and laboratory studies, Aust. J. Soil Res. **30**, 429 (1992).
[2] E. Shimojima, R. Yoshioka, and I. Tamagawa, Salinization owing to evaporation from bare-soil surfaces and its influences on the evaporation, J. Hydrol. **178**, 109 (1996).
[3] H. Derluyn, P. Moonen, and J. Carmeliet, Deformation and damage due to drying-induced salt crystallization in porous limestone, J. Mech. Phys. Solids **63**, 242 (2014).
[4] B. Lubelli, R. P. J. van Hees, and C. J. W. P. Groot, The role of sea salts in the occurrence of different damage mechanisms and decay patterns on brick masonry, Constr. Build. Mater. **18**, 119 (2004).
[5] P. Rengasamy, World salinization with emphasis on Australia, J. Exp. Bot. **57**, 1017 (2006).
[6] N. Shokri, P. Lehmann, and D. Or, Critical evaluation of enhancement factors for vapor transport through unsaturated porous media, Water Resour. Res. **45**, W10433 (2009).
[7] J. R. Phillip and D. A. de Vries, Moisture movement in porous materials under temperature gradients, Trans. Am. Geophys. Union **38**, 222 (1957).
[8] N. Vorhauer, E. Tsotsas, and M. Prat, Temperature gradient induced double stabilization of the evaporation front within a drying porous medium, Phys. Rev. Fluids **3**, 114201 (2018).
[9] O. A. Plumb, L. Gu, and S. W. Webb, Drying of porous materials at low moisture content, Drying Technol. **17**, 1999 (1999).
[10] W. J. P. van Enckevort and J. H. Los, On the creeping of saturated salt solutions, Cryst. Growth Des. **13**, 1838 (2013).
[11] M. J. Qazi, H. Salim, C. A. W. Doorman, E. Jambon-Puillet, and N. Shahidzadeh, Salt creeping as a self-amplifying crystallization process, Sci. Adv. **5**, eaax1853 (2019).
[12] A. G. Yiotis, D. Salin, E. S. Tajer, and Y. C. Yortsos, Drying in porous media with gravity-stabilized fronts: Experimental results, Phys. Rev. E **86**, 026310 (2012).
[13] R. J. Millington and J. P. Quirk, Permeability of porous solids, Trans. Faraday Soc. **57**, 1200 (1961).
[14] L. Pel, R. Pishkari, and M. Casti, A simplified model for the combined wicking and evaporation of a NaCl solution in limestone, Mater. Struct. **51**, 66 (2018).
[15] U. Nachshon, N. Weisbrod, R. Katzir, and A. Nasser, NaCl crust architecture and its impact on evaporation: Three-dimensional insights, Geophys. Res. Lett. **45**, 6100 (2018).
[16] S. Dai, H. Shin, and J. C. Santamarina, Formation and development of salt crusts on soil surfaces, Acta Geotech. **11**, 1103 (2016).
[17] G. Licsandru, C. Noiriel, S. Geoffroy, A. Abou-Chakra, P. Duru, and M. Prat, Detachment mechanism and reduced evaporation of an evaporative NaCl salt crust, Sci. Rep. **12**, 7473 (2022).
[18] G. Licsandru, C. Noiriel, P. Duru, S. Geoffroy, A. Abou Chakra, and M. Prat, Dissolution-precipitation-driven upward migration of a salt crust, Phys. Rev. E **100**, 032802 (2019).
[19] H. Eloukabi, N. Sghaier, S. Ben Nasrallah, and M. Prat, Experimental study of the effect of sodium chloride on drying of porous media: The crusty-patchy efflorescence transition, Int. J. Heat Mass Transfer **56**, 80 (2013).
[20] S. Veran-Tissoires and M. Prat, Evaporation of a sodium chloride solution from a saturated porous medium with efflorescence formation, J. Fluid Mech. **749**, 701 (2014).
[21] M. N. Rad, N. Shokri, and M. Sahimi, Pore-scale dynamics of salt precipitation in drying porous media, Phys. Rev. E **88**, 032404 (2013).
[22] M. N. Rad and N. Shokri, Effects of grain angularity on NaCl precipitation in porous media during evaporation, Water Resour. Res. **50**, 9020 (2014).
[23] N. Sghaier and M. Prat, Effect of efflorescence formation on drying kinetics of porous media, Transp. Porous Media **80**, 441 (2009).
[24] H. Fujimaki, T. Shimano, M. Inoue, and K. Nakane, Effect of a salt crust on evaporation from a bare saline soil, Vadose Zone J. **5**, 1246 (2006).
[25] J. Desarnaud, H. Derluyn, L. Molari, S. de Miranda, V. Cnudde, and N. Shahidzadeh, Drying of salt contaminated porous media: Effect of primary and secondary nucleation, J. Appl. Phys. **118**, 114901 (2015).
[26] M. Prat, Recent advances in pore-scale models for drying of porous media, Chem. Eng. J. **86**, 153 (2002).

[27] M. Talbi and M. Prat, Coupling between internal and external mass transfer during stage-1 evaporation in capillary porous media: Interfacial resistance approach, Phys. Rev. E **104**, 055102 (2021).
[28] A. L. Dullien, C. Zarcone, I. F. Macdonald, A. Collins, and R. D. E. Bochard, The effects of surface roughness on the capillary pressure curves and the heights of capillary rise in glass bead packs, J. Colloid Interface Sci. **127**, 362 (1989).
[29] H. P. Huinink, L. Pel, and M. A. J. Michels, Structure and transport properties of liquid clusters in a drying porous medium, Phys. Rev. E **68**, 056114 (2003).
[30] J. Desarnaud, H. Derluyn, J. Carmeliet, D. Bonn, and N. Shahidzadeh, Metastability limit for the nucleation of nacl crystals in confinement, J. Phys. Chem. Lett. **5**, 890 (2014).
[31] P. Duru A. Naillon, M. Marcoux, and M. Prat, Evaporation with sodium chloride crystallization in a capillary tube, J. Cryst. Growth **422**, 52 (2015).
[32] U. Nachshon, N. Weisbrod, M. Dragila, and A. Grader, Combined evaporation and salt precipitation in homogeneous and heterogeneous porous media, Water Resour. Res. **47**, W03513 (2011).
[33] H. Salim, P. Kolpakov, D. Bonn, and N. Shahidzadeh, Self-lifting NaCl crystals, J. Phys. Chem. Lett. **11**, 7388 (2020).
[34] S. A. McBride, H.-L. Girard, and K. K. Varanasi, Crystal critters: Self-ejection of crystals from heated, superhydrophobic surfaces, Sci. Adv. **7**, eabe6960 (2021).
[35] H. P. Huinink, L. Pel, and M. A. J. Michels, How ions distribute in a drying porous medium: A simple model, Phys. Fluids **14**, 1389 (2002).
[36] M. Prat, N.Sghaier, and S. Ben Nasrallah, On ions transport during drying in a porous medium, Transp. Porous Media **67**, 243 (2007).